# Radiotracers to Address Unmet Clinical Needs in Cardiovascular Imaging, Part 1: Technical Considerations and Perfusion and Neuronal Imaging

John C. Stendahl*[1], Jennifer M. Kwan*[1], Darko Pucar[2], and Mehran M. Sadeghi[1,3]

[1]Section of Cardiovascular Medicine, Yale University School of Medicine, New Haven, Connecticut; [2]Department of Radiology and Biomedical Imaging, Yale University School of Medicine, New Haven, Connecticut; and [3]Veterans Affairs Connecticut Healthcare System, West Haven, Connecticut

**Learning Objectives:** On successful completion of this activity, participants should be able to describe (1) key technical considerations pertaining to cardiovascular radiotracer development; (2) basic concepts in cardiac and peripheral perfusion imaging and associated radiotracers; and (3) basic concepts in cardiovascular neuronal imaging and associated radiotracers.

**CME Credit:** SNMMI is accredited by the Accreditation Council for Continuing Medical Education (ACCME) to sponsor continuing education for physicians. SNMMI designates each *JNM* continuing education article for a maximum of 2.0 AMA PRA Category 1 Credits. Physicians should claim only credit commensurate with the extent of their participation in the activity. For CE credit, SAM, and other credit types, participants can access this activity through the SNMMI website (http://www.snmmilearningcenter.org) through May 2025.

The development of new radiotracers for PET and SPECT is central to addressing unmet diagnostic needs related to systemwide trends toward molecular characterization and personalized therapies in cardiovascular medicine. In the following 2-part review, we discuss select emerging radiotracers that may help address important unmet diagnostic needs in central areas of cardiovascular medicine, such as heart failure, arrhythmias, valvular disease, atherosclerosis, and thrombosis. Part 1 examines key technical considerations pertaining to cardiovascular radiotracer development and reviews emerging radiotracers for perfusion and neuronal imaging. Highlights of this work include discussions on the development of ^{18}F-flurpiridaz, an emerging PET perfusion tracer, and the development of ^{18}F-based radiotracers for cardiovascular neuronal imaging, such as ^{18}F-fluorobenguane. Part 2 of this review covers emerging radiotracers for the imaging of inflammation, fibrosis, thrombosis, calcification, and cardiac amyloidosis.

**Key Words:** cardiology (basic/technical); cardiology (clinical); molecular imaging; inflammation; myocardial perfusion imaging

Despite considerable progress in patient care, cardiovascular disease remains a major cause of morbidity and mortality. Improved diagnostics, treatments, and risk factor management have altered the landscape of patient care and have likely contributed to the increasing prevalence of chronic cardiovascular disease. For example, the number of patients living with heart failure is expected to increase from 5.8 million in 2012 to 8.5 million in 2030 (*1*). This evolution of patient demographics and an improved understanding of cardiovascular pathophysiology underpin many current diagnostic and risk stratification gaps in cardiovascular medicine. Emerging molecular imaging techniques have the potential to address many of these unmet needs (Table 1).

Myocardial perfusion imaging, myocardial viability imaging, and equilibrium radionuclide angiocardiography have traditionally constituted most nuclear cardiology procedures. However, use patterns in nuclear cardiology laboratories have been changing because of advances in molecular imaging, the emergence of alternative diagnostic techniques, and evolving evidence questioning established approaches to diagnose and risk-stratify coronary artery disease. PET and SPECT have several advantages for physiologic and precision molecular applications in cardiovascular imaging, including their sensitivity, versatility, and quantitative nature. This is evident in the fact that PET- and SPECT-based molecular imaging techniques are now routinely performed clinically for the diagnosis of cardiac sarcoidosis and amyloidosis. Moreover, the feasibilities of neurohormonal and device infection imaging have been demonstrated, although their specific roles in patient management remain to be established. Many additional cardiovascular applications of PET and SPECT are in earlier stages of preclinical and clinical development, and their advancement to mainstream clinical use is critically dependent on the physical, chemical, and biologic properties of their radiotracers.

In the following 2-part review, we discuss select emerging radiotracers that may help address key unmet clinical diagnostic needs in cardiovascular medicine. For simplicity, these tracers are organized by general pathobiologic processes rather than specific diseases. Part 1 of

**TABLE 1**
Unmet Diagnostic Needs in Cardiovascular Medicine

| Clinical field | Unmet need |
| --- | --- |
| Heart failure and cardiomyopathies | Heart failure with preserved ejection fraction: phenotypic characterization, therapeutic development |
| | Heart failure with reduced ejection fraction: prognostication, precision approaches to therapy |
| | Post–myocardial infarction remodeling: prognostication |
| | Immunotherapy/chemotherapy-related cardiotoxicity: prediction, early recognition, prognostication, and assessment of treatment response |
| | Cardiac amyloidosis: single-scan diagnosis and typing (light-chain amyloidosis vs. transthyretin amyloidosis) |
| | Cardiac sarcoidosis: reduce dependence on dietary preparation, differentiate from other types of myocarditis/nonspecific uptake |
| | Genetic cardiomyopathies: risk stratification in asymptomatic or phenotype-negative carriers and those carrying variants of unknown significance |
| | Cardiac fibrosis: reproducible quantification, distinguish between active and stable disease |
| | Left ventricular assist devices: prediction of left ventricular myocardial recovery |
| | New medical therapies (e.g., angiotensin receptor neprilysin inhibitors, sodium glucose cotransporter 2 inhibitors): determination of mechanism of action, track therapeutic response |
| Arrhythmias | Sudden cardiac death: risk stratification, prediction of implantable cardiac defibrillator benefit |
| | Genetic arrhythmia syndromes: risk stratification in asymptomatic or phenotype-negative carriers and those carrying variants of unknown significance |
| | Atrial fibrillation: patient selection for ablation/cardioversion/antiarrhythmic drugs |
| Valvular disease | Valvular regurgitation/stenosis: determination of risk for progression, prediction of optimal timing of interventions, selection for medical therapy, tracking of therapeutic response |
| | Endocarditis or device infections: detection |
| Vascular disease | Atheroma: risk stratification |
| | Aortic aneurysm: risk stratification, prediction of endoleak |
| | Thrombosis or embolization: whole-body detection, determination of chronicity |
| | Perfusion: high-spatial-resolution imaging with absolute blood flow quantification, hybrid perfusion/angiographic imaging |
| | Peripheral artery disease: risk stratification, prediction of interventional benefit |

the review examines key technical considerations pertaining to cardiovascular radiotracer development and reviews the development of radiotracers for perfusion and neuronal imaging (Table 2). Part 2 covers emerging radiotracers for the imaging of inflammation, fibrosis, thrombosis, calcification, and cardiac amyloidosis.

## TECHNICAL CONSIDERATIONS FOR OPTIMAL NUCLEAR CARDIOVASCULAR IMAGING

Multiple variables related to radiotracers, instrumentation, and image analysis contribute to the generation of useful nuclear imaging data. PET offers several distinct advantages over SPECT for cardiovascular imaging, including greater spatial resolution and more established quantification methods (2). However, SPECT is usually less expensive and more widely available in clinical nuclear cardiology laboratories. With recent improvements in SPECT technology such as cardiorespiratory gating and cadmium-zinc-telluride (CZT) detectors (3–5), differences between the 2 modalities may be less significant. One potential advantage of SPECT over PET in cardiovascular molecular imaging is its capability for simultaneous

multitracer imaging (Fig. 1) (4,6–8). CZT SPECT cameras facilitate multitracer imaging by providing greater spatial and energy resolution than traditional Anger cameras (5).

Cardiac imaging with PET and SPECT is facilitated by the large size of the organ, although motion remains a challenge. Vascular imaging presents additional challenges, including the small size of vessels. This may be addressed by hybrid imaging with CT or MRI, which provides anatomic definition and helps to correct partial-volume effects. Cardiovascular molecular imaging applications would benefit from improved quantitation tools, as the semiquantitative techniques developed for perfusion imaging to assess relative radiotracer uptake are not suitable for hot-spot imaging, which is common in molecular imaging applications.

Radiotracer kinetics govern acquisition protocols and greatly influence data quality. Fast blood pool clearance is desirable for most non–blood pool cardiovascular applications because it improves target-to-background ratios. For perfusion imaging, it is desirable to have high levels of target tissue extraction and retention, with lesser uptake or greater washout in surrounding organs. For molecular imaging,

**TABLE 2**
Select Perfusion and Neuronal Signaling Radiotracers in Cardiovascular Medicine

| Application | Radiotracer | Mechanism/target | Status | Reference |
|---|---|---|---|---|
| Perfusion | ^{18}F-flurpiridaz | Mitochondrial complex 1 | Phase 3 clinical | (10,13–16) |
| | ^{18}F-rhodamine 6G | Mitochondrial membrane voltage sensor | Initial clinical evaluations | (20) |
| | ^{18}F-fluorophenyltriphenylphosphonium | Mitochondrial membrane voltage sensor | Initial clinical evaluations | (21) |
| | ^{123}I-CMICE-013 | Mitochondrial complex 1 | Initial clinical evaluations | (22) |
| | ^{123}I-ZIROT | Mitochondrial complex 1 | Preclinical | (23) |
| Neuronal signaling | | | | |
| *Presynaptic* | | | | |
| | ^{123}I-MIBG | Norepinephrine transporter | FDA-approved for prognostication in heart failure | (35,38,39,45,61) |
| | ^{11}C-HED | Norepinephrine transporter | Clinical evaluations | (34,36,37,48,49) |
| | ^{11}C-epinephrine | Norepinephrine transporter | Initial clinical evaluations | (48) |
| | ^{11}C-phenylephrine | Norepinephrine transporter | Initial clinical evaluations | (48) |
| | ^{18}F-FBBG | Norepinephrine transporter | Initial clinical evaluations | (54,55) |
| | [18]F-4F-MHPG, [18]F-3F-PHPG | Norepinephrine transporter | Initial clinical evaluations | (58) |
| | ^{18}F-MFBG | Norepinephrine transporter | Initial clinical evaluations | (56,57) |
| *Postsynaptic* | | | | |
| | ^{11}C-CGP-12177, ^{11}C-CGP-12388 | β-receptor antagonists | Initial clinical evaluations | (37,49,59–61) |
| | ^{11}C-GB67 | α1-receptor antagonist (prazosin analog) | Initial clinical evaluations | (63,64) |
| *Parasympathetic* | | | | |
| | ^{11}C-donepezil | Acetylcholinesterase antagonist | Initial clinical evaluations | (65) |
| | ^{11}C-methylquinuclidinyl benzilate | Muscarinic receptor antagonist | Initial clinical evaluations | (40) |
| | 2-deoxy-2-^{18}F-fluoro-D-glucose-A85380 | Selective $\alpha_4\beta_2$ nicotinic receptor agonist | Initial clinical evaluations | (67) |
| | ^{18}F-fluoroethoxybenzovesamicol | Vesicular acetylcholine transporter | Initial clinical evaluations | (69) |

[18]F-4F-MHPG = 4-^{18}F-fluoro-meta-hydroxyphenethylguanidine; [18]F-3F-PHPG = 3-^{18}F-fluoro-para-hydroxyphenethylguanidine; FDA = Food and Drug Administration.
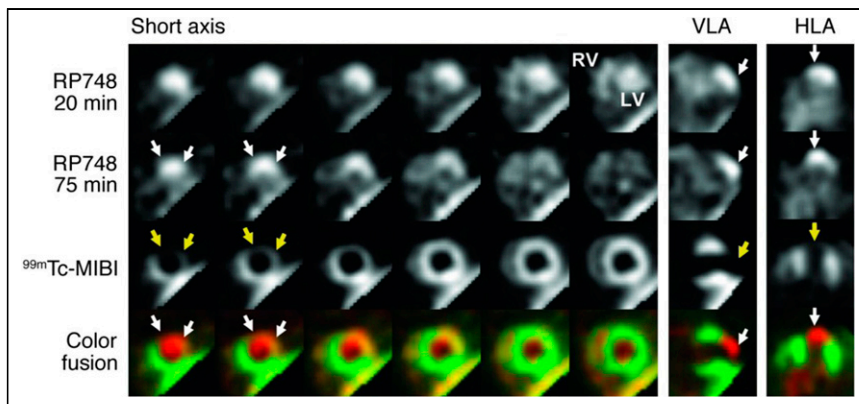
**FIGURE 1.** Dual-tracer SPECT imaging of postmyocardial infarction angiogenesis in a canine model using [111]I-RP748, an $\alpha_v\beta_3$ integrin–targeted agent. Shown are in vivo ^{111}In-RP748 SPECT images acquired at 20 and 45min after tracer administration (top 2 rows), ^{99m}Tc-sestamibi images (third row), and fused ^{99m}Tc-sestamibi (green) and 45-min [11]In-RP748 (red) images (bottom row) in a dog 3 wk after left anterior descending coronary artery occlusion. ^{99m}Tc-sestamibi perfusion images demonstrate anterior perfusion deficit (yellow arrows). ^{111}In-RP748 images demonstrate corresponding increased uptake in hypoperfused region (white arrows). Authors demonstrate that 4-fold increase in ^{111}In-RP748 uptake in infarct region corresponds to increased $\alpha_v\beta_3$ expression and histologic evidence of angiogenesis. LV = left ventricle; MIBI = sestamibi; RV = right ventricle; VLA = vertical long axis; HLA = horizontal long axis. (Reprinted with permission of (8).)

high levels of specific target binding relative to the background are critical for achieving useful data. In this regard, radiotracer uptake depends on delivery of the tracer as well as target expression and binding affinity, thus raising challenges for comparing uptake values, such as in areas of myocardium with differing levels of perfusion. The incorporation of regional perfusion data from kinetic modeling could potentially improve the accuracy of molecular imaging techniques.

The chemical and physical properties of radionuclides also influence synthesis and acquisition protocols and affect data quality (Table 3). Radionuclide chemical properties impact their incorporation into organic tracer molecules or, in the case of inorganic radiotracers (e.g., [82]Rb), their biologic uptake (9). Radionuclides with shorter half-lives are ideally suited for applications with faster pharmacokinetics and favorable count statistics. Shorter half-lives reduce radiation exposure to both patients and staff and typically permit greater imaging throughput. This advantage is especially useful in perfusion imaging to minimize delays between stress and rest scans. However, radionuclides with shorter half-lives are not always practical. For example, radiolabeled antibodies have slower pharmacokinetics than small molecules, and their binding to target molecules with low levels of expression can require hours to produce high-quality signals. As such, molecular imaging with antibodies often necessitates the use of radionuclides with a longer half-life, such as [64]Cu (half-life, 12.7 h) or [89]Zr (half-life, 78.4 h). Radionuclides with longer half-lives can also provide considerable procedural flexibility. For example, radionuclides with a longer half-life facilitate unit dose delivery in place of on-site generators and cyclotrons, which may not be cost-effective in lower-volume centers (10). Longer–half-life radionuclides also expand options for chemical modifications to radiotracers before administration. For myocardial perfusion imaging, longer–half-life radionuclides permit exercise stress (10) and may be favorable for nontraditional applications such as image-guided interventions (11). However, greater radiation exposure associated with these longer–half-life radionuclides and practical workflow considerations remain major limiting factors for cardiovascular applications, where risk–benefit

considerations may be different from, for example, imaging in patients with malignancies. In PET imaging, radionuclide positron energy influences image resolution. Lower-energy $\beta$-emitters such as ^{18}F and ^{64}Cu have shorter positron ranges in tissue and thus tend to produce images with spatial resolution superior to that of higher-energy positron emitters such as [82]Rb and [68]Ga (12). The benefits of high-resolution imaging are the greatest in small targets that are more susceptible to partial-volume effects, such as vessel walls. With anticipated improvements in resolution related to PET camera technology and motion correction, the effects of radionuclide positron range will likely become increasingly significant.

The mode of decay of radionuclides also affects their imaging properties. PET radionuclides such as ^{11}C, ^{13}N, ^{15}O, and ^{18}F are pure $\beta^+$-emitters and do not directly produce $\gamma$- or $\beta^-$-emissions (9,12). Prompt $\gamma$-emissions from nonpure PET radionuclides such as ^{68}Ga, [82]Rb, and [124]I have traditionally been considered unfavorable because they increase radiation exposure and create spurious coincidences that degrade image quality (12). However, the presence of smaller levels of prompt $\gamma$-emissions in radionuclides with other favorable properties is not considered prohibitive, and image quality can potentially be improved by instituting corrections (12). Moreover, it has been proposed that radionuclides emitting prompt $\gamma$-emissions provide distinct emission signatures that could be harnessed for multitracer PET imaging (12).

## RADIOTRACERS FOR PERFUSION IMAGING

There has been longstanding interest in the development of ^{18}F-based perfusion tracers given the intrinsic advantages of PET imaging and the limitations of current clinical perfusion tracers such as ^{99m}Tc sestamibi, ^{99m}Tc tetrofosmin, [82]Rb, and ^{13}N-NH$_3$ (13). [18]F is advantageous because it has a shorter mean positron range (0.6 mm, in water) than [82]Rb (7.1 mm) and [13]N (1.8 mm) and thus provides superior spatial resolution (12). In addition, ^{18}F has a longer half-life (109 min) than [82]Rb (76 s) and [13]N (10 min). Although this characteristic can be unfavorable from a dosimetric standpoint and may necessitate greater delays between rest and stress acquisitions, it also provides several distinct advantages. Most importantly, the longer half-life of ^{18}F permits unit dose delivery. In addition, the longer half-life of ^{18}F permits both exercise and pharmacologic stress protocols and makes repeat image acquisition possible in cases of motion or extracardiac radiotracer uptake.

[18]F-flurpirdaz is a perfusion tracer that binds to mitochondrial complex 1 and is currently undergoing evaluation in clinical trials (10,13–17). In addition to the features listed above, ^{18}F-flurpiridaz has greater myocardial extraction at higher blood flow rates than traditional PET and SPECT perfusion radiotracers; thus, its uptake demonstrates a smaller deviation from linearity over the physiologic range of blood flow (Fig. 2) (18). This property potentially improves its sensitivity for detection of ischemia and is advantageous for quantification of absolute blood flow. In a recent phase 3 clinical evaluation, ^{18}F-flurpiridaz PET demonstrated increased sensitivity for the detection of obstructive coronary artery disease

## TABLE 3
### Properties of SPECT and PET Radionuclides with Existing or Potential Applications in Cardiovascular Imaging (9,12,70)

| Radionuclide | Production | Half-life | Decay (%) | $E_{\beta+ \, max}$ (MeV) | $R_{\beta+ \, mean}$ (mm) | $E_\gamma$ (MeV) |
|---|---|---|---|---|---|---|
| **γ-emitters (SPECT)** | | | | | | |
| $^{99m}$Tc | Generator ($^{99}$Mo) | 6.0 h | IT (88), IC | — | — | 0.141 |
| $^{201}$Tl | Cyclotron | 73.1 h | EC | — | — | 0.068–0.083* |
| $^{123}$I | Cyclotron | 13.2 h | EC (87), IC | — | — | 0.159† |
| **Pure positron emitters (PET)** | | | | | | |
| $^{15}$O | Cyclotron | 2 min | $\beta^+$ (99.9) | 1.732 | 3.0 | — |
| $^{13}$N | Cyclotron | 10.0 min | $\beta^+$ (99.8) | 1.199 | 1.8 | — |
| $^{11}$C | Cyclotron | 20.4 min | $\beta^+$ (99.8) | 0.960 | 1.2 | — |
| $^{18}$F | Cyclotron | 110 min | $\beta^+$ (96.9) | 0.634 | 0.6 | — |
| **Mixed emitters (PET)** | | | | | | |
| $^{64}$Cu | Cyclotron | 12.7 h | $\beta^+$ (17.5)/EC | 0.653 | 0.7 | — |
| | | | $\beta^-$ (38.5) | — | — | — |
| $^{89}$Zr | Cyclotron | 78.4 h | $\beta^+$ (22.7)/EC | 0.902 | 1.3 | 0.909‡ |
| $^{82}$Rb | Generator ($^{82}$Sr) | 1.3 min | $\beta_1^+$ (81.8) | 3.378 | 7.1 | — |
| | | | $\beta_2^+$ (13.1)/EC | 2.601 | 5.0 | 0.777 |
| $^{68}$Ga | Generator ($^{68}$Ge) | 68 min | $\beta_1^+$ (87.7) | 1.899 | 3.5 | — |
| | | | $\beta_2^+$ (1.2)/EC | 0.821 | 1.1 | 1.077 |
| $^{124}$I | Cyclotron | 100.2 h | $\beta_1^+$ (11.7)/EC | 1.535 | 2.8 | 0.602 |
| | | | $\beta_2^+$ (10.7) | 2.138 | 4.4 | — |
| | | | $\beta_3^+$ (0.3)/EC | 0.812 | 1.1 | 0.723 |
| | | | EC | — | — | 1.691 |

$E_{\beta+ \, max}$ = maximum energy of positrons; $R_{\beta+ \, mean}$ = mean range of positrons in water; $E_\gamma$ = γ emission energy; IT = isomeric transition; IC = internal conversion; EC = electron capture.

*Nongaussian photopeak.

†Emits small proportions of high-energy γ-photons (>0.400 MeV) in addition to its primary emission at 0.159 MeV.

‡Does not behave as prompt γ because of long half-life of metastable intermediate.

(as defined by >50% coronary stenosis by invasive angiography) in comparison to $^{99m}$Tc-SPECT (71.9% vs. 53.7%, $P < 0.001$) but did not meet the predetermined noninferiority criterion pertaining to specificity (76.2% vs 86.6%, $P$ = not significant) (10). Overall, on the basis of area under the receiver-operating-characteristic curve, $^{18}$F-flurpiridaz PET demonstrated superior discrimination of obstructive coronary disease in comparison to $^{99m}$Tc-SPECT myocardial perfusion imaging (0.78 vs. 0.72, $P < 0.001$). $^{18}$F-flurpiridaz also exhibited better image quality than $^{99m}$Tc-SPECT at lower radiation doses (6.1 ± 0.4 vs. 13.4 ± 3.2 mSv; $P < 0.001$) (10). Of note, this comparison was based solely on retention scans and did not incorporate $^{18}$F-flurpiridaz myocardial blood flow quantification (19). It is also worth noting that this study did not compare $^{18}$F-flurpiridaz with other PET perfusion tracers and that at least some of the differences likely represent intrinsic differences between SPECT and PET techniques, including a lack of attenuation correction for SPECT images. The effects of spatial resolution in $^{18}$F-flurpiridaz PET were further illustrated in a subsequent analysis of the trial data that compared diagnostic performance in large and small ventricles. The diagnostic performance of $^{18}$F-flurpiridaz PET for the detection of ischemia was similar in large and small left ventricles (area under the curve, 0.79 vs. 0.77, $P = 0.49$), but $^{99m}$Tc-SPECT performance was reduced in smaller left ventricles (area under the curve, 0.75 vs. 0.67, $P = 0.03$),

likely because of its lower spatial resolution (Fig. 3) (17). Other $^{18}$F-based PET perfusion tracers that are undergoing initial characterization and evaluation in humans include $^{18}$F-rhodamine 6G (NCT04528758) (20) and $^{18}$F-fluorophenyltriphenylphosphonium (NCT02252783) (21).

Several new SPECT perfusion agents are also in development, including the $^{123}$I-labeled rotenone derivatives $^{123}$I-CMICE-013 (22) and $^{123}$I-ZIROT (23). These agents target mitochondrial complex 1 in a similar fashion to $^{18}$F-flurpiridaz and are intended to address the shortcomings of existing SPECT perfusion agents by potentially combining the benefits of greater myocardial extraction across the physiologic range of blood flow, with favorable imaging characteristics and dosimetry. Moreover, as these agents are labeled with $^{123}$I rather than $^{99m}$Tc, they could also address ongoing concerns about the stability of the $^{99m}$Tc supply. In initial preclinical studies on pigs, $^{123}$I-CMICE-013 demonstrated greater myocardial uptake than the conventional SPECT tracers $^{201}$Tl, $^{99m}$Tc-tetrofosmin, and $^{99m}$Tc-sestamibi at blood flows exceeding 1.5 mL/min/g ($P < 0.05$) (Fig. 4) (22). Similarly, $^{123}$I-ZIROT demonstrated greater myocardial uptake than $^{201}$Tl and $^{99m}$Tc-sestamibi at blood flows greater than 1.5 mL/min/g, with linear uptake extending to greater flow values (23). $^{123}$I-CMICE-013 recently completed a phase 1 clinical evaluation (NCT01558362). One potential technical issue with $^{123}$I-based perfusion agents is that $^{123}$I emits small proportions of high-energy photons (>400 keV) in addition to its primary emission at 159 keV. These
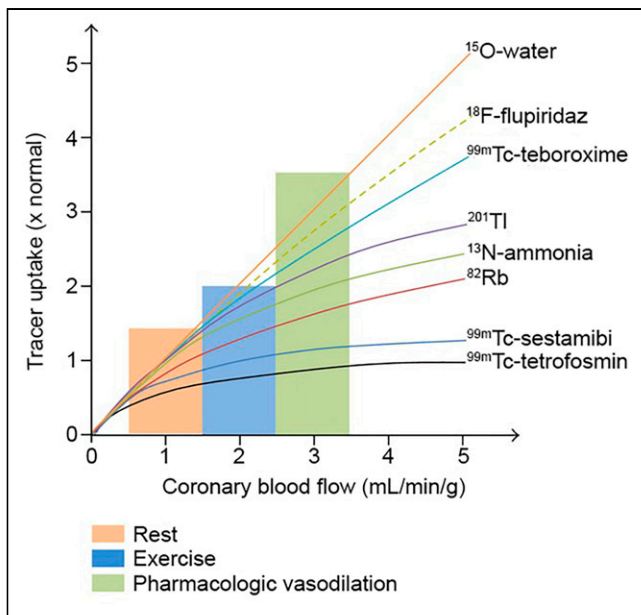
**FIGURE 2.** Schematic representation of myocardial uptake of various PET and SPECT perfusion radiotracers in relation to coronary blood flow. Background colors in figure show typical ranges of myocardial blood flow during rest (peach), exercise stress (blue), and pharmacologic vasodilator stress (green). $^{15}O$-$H_2O$ displays nearly linear uptake over physiologic range of blood flow but has limited clinical utility because of suboptimal imaging characteristics. $^{18}F$-flurpiridaz maintains high levels of myocardial extraction at stress-level blood flows, and its uptake-flow curve thus demonstrates only minimal deviation from linearity. By contrast, $^{99m}Tc$-sestamibi and $^{99m}Tc$-tetrofosmin have more significant reductions in myocardial extraction at moderate and high blood flow rates, and their uptake-flow curves demonstrate significant deviations from linearity. $^{201}Tl$, $^{13}N$-$NH_3$, and $^{82}Rb$ have intermediate uptake-flow properties. (Reprinted from ([18]).)

high-energy photons can degrade image quality and impair quantitative analyses by penetrating septa on standard low-energy, high-resolution collimators. Collimators with thicker septa may be used in $^{123}I$ SPECT imaging to decrease septal photon penetration, although thicker septa tend to decrease spatial resolution ([24]).

Despite the trend toward greater use of PET for perfusion imaging, improved SPECT radiotracers may still have a significant

clinical impact, as SPECT myocardial perfusion imaging is expected to continue being the most common perfusion modality for years to come because of advantages in cost and availability. Moreover, with technologic advances such as attenuation correction ([25]) and CZT detectors ([5]), modern SPECT imaging systems provide substantially better image quality at a more favorable dosimetry than prior-generation instruments. The combination of advances in instrumentation and the development of perfusion tracers with better myocardial extraction characteristics also raises the possibility of applying SPECT-based quantitative blood flow assessments in clinical settings ([26]).

A potentially significant area for growth and possible application for these new perfusion agents is skeletal muscle perfusion imaging. Peripheral artery disease affects more than 200 million people worldwide ([27]) and presents significant challenges for clinical assessment and treatment. SPECT and PET perfusion imaging with traditional radiotracers has been applied to help diagnose peripheral artery disease, stratify risk, and evaluate responses to treatment ([28–31]). Although not currently part of mainstream clinical peripheral artery disease management, radiotracer imaging techniques may provide supplemental information to better assess risk for acute limb ischemia and potential for wound healing, as well as to direct optimal approaches for revascularization. The high spatial resolution, quantitative potential, and ability to accommodate exercise stress protocols are features of the new $^{18}F$-based tracers that make them attractive for peripheral perfusion applications.

## RADIOTRACERS FOR CARDIOVASCULAR NEURONAL IMAGING

Neuronal signaling in the myocardium plays a critical role in maintaining cardiac function and homeostasis by modulating electromechanical behavior, vasoreactivity, metabolism, and remodeling ([32]). Neuronal signals are transmitted to the heart via the sympathetic and parasympathetic branches of the autonomic nervous system. Sympathetic activation of the heart has mainly stimulatory effects, including increased inotropy and chronotropy ([32]). Preganglionic sympathetic neurons originate in the spinal cord and transmit signals to postganglionic fibers that innervate the atria, ventricles, and coronary arteries. On stimulation, the termini of these postganglionic neurons release stored norepinephrine into the synaptic cleft. Sympathetic effects are mediated by binding of
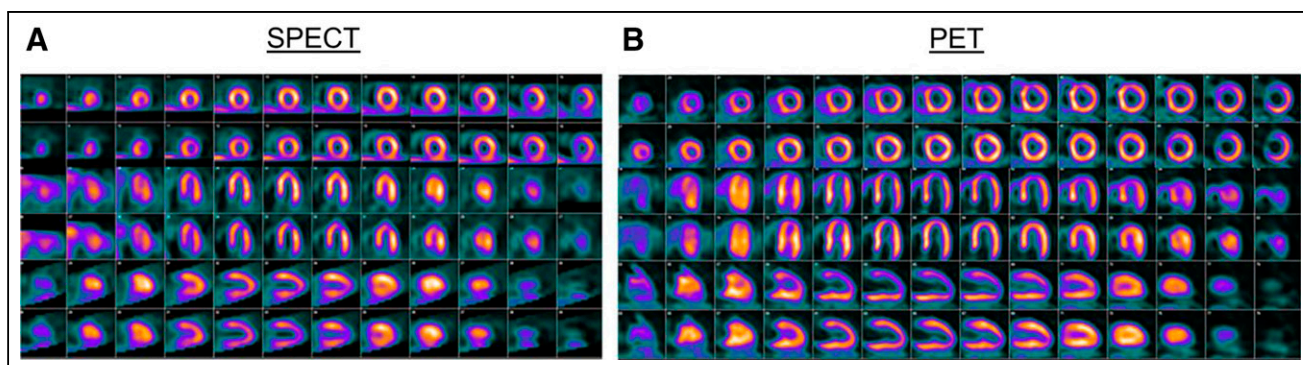


**FIGURE 3.** Representative rest–stress $^{99m}Tc$-SPECT and $^{18}F$-flurpiridaz PET images in patient with small heart. Images were acquired in 66-y-old woman with left ventricular end diastolic volume of 82 mL. Reversible anterior perfusion defect is more evident in $^{18}F$-flurpiridaz PET images (B) than $^{99m}Tc$-SPECT images (A) and is consistent with 82% stenosis of left anterior descending coronary artery that was found on invasive coronary angiography. Greater sensitivity of $^{18}F$-flurpiridaz PET for detection of myocardial ischemia partially relates to its greater spatial resolution and more linear uptake over physiologic range of blood flow. (Reprinted from ([17]).)
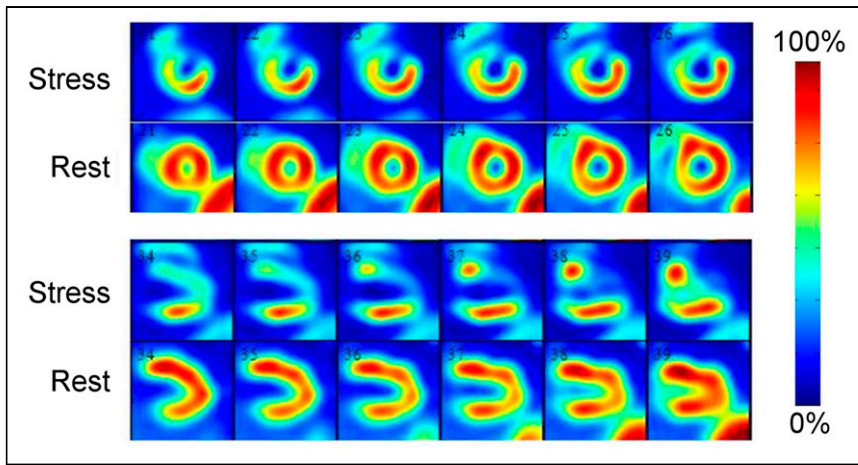
**FIGURE 4.** Representative $^{123}$I-CMICE-013 SPECT perfusion images in a porcine model with left anterior descending coronary artery occlusion during dipyridamole stress. Images were acquired 15 min after injection and provide clear definition of occluded region. (Reprinted from (22).)

norepinephrine to postsynaptic α- and β-adrenergic receptors in the cardiac tissue. In contrast, parasympathetic activation tends to be inhibitory, with negative chronotropic and, to a lesser extent, negative inotropic effects (32). Parasympathetic signals are transmitted from the medulla oblongata to the heart by way of the vagus nerve. The termini of postganglionic vagal efferents are concentrated in the atria and conduction nodes and release acetylcholine when stimulated. Signal transmission is completed by binding of acetylcholine to muscarinic and nicotinic receptors. Muscarinic acetylcholine receptors are present in cardiomyocytes and intracardiac ganglia, and their stimulation decreases both inotropy and chronotropy (33). Nicotinic acetylcholine receptors are present in the myocardium and vasculature, although their roles are less well defined (33). In addition to efferent sympathetic and parasympathetic innervation of the heart, there are numerous afferent sympathetic and vagal nerve fibers that travel from the heart for sensory purposes and to mediate cardiac reflexes.

Alterations to cardiac neuronal activity play important roles in the pathophysiology of arrythmias, myocardial infarction, and heart failure related to various types of cardiomyopathy (34–42). In the case of heart failure, it is postulated that chronically elevated sympathetic activity drives desensitization or downregulation of both presynaptic norepinephrine reuptake transporters and postsynaptic β-adrenergic receptors, which leads to progressive dysfunction and remodeling and creates substrates for arrhythmias (43). The development of radiotracers for targeted noninvasive imaging of various aspects of cardiac innervation has improved our understanding of complex cardiovascular diseases and has helped to guide treatments. Recent efforts in the field have focused on developing new tracers and improving image acquisition and analysis techniques to expand diagnostic capabilities and provide more accurate and reproduceable assessments (44).

**Presynaptic Sympathetic Imaging**

$^{123}$I-metaiodobenzylguanidine ($^{123}$I-MIBG) targets the norepinephrine transporter and was the first neuronal radiotracer to be extensively studied in hearts and Food and Drug Administration–approved for cardiac applications. Myocardial $^{123}$I-MIBG uptake can be imaged by both planar scintigraphy and SPECT/CT, although quantification has traditionally been performed with heart-to-mediastinum ratios in planar images. Reduced myocardial uptake of $^{123}$I-MIBG has been associated with various cardiac diseases and has demonstrated clinical predictive

value. In the ADMIRE-HF trial (AdreView Myocardial Imaging for Risk Evaluation in Heart Failure) of patients with heart failure with reduced ejection fraction, a $^{123}$I-MIBG heart-to-mediastinum ratio of at least 1.6 was predictive of decreased adverse outcomes such as heart failure progression (hazard ratio, 0.49; $P = 0.002$), serious arrhythmic events (hazard ratio, 0.37; $P = 0.020$), and cardiac death (hazard ratio, 0.14; $P = 0.006$) as compared with a heart-to-mediastinum ratio of less than 1.6 (35). Although $^{123}$I-MIBG has been criticized because assessments are often global and semiquantitative (45), improved SPECT technology such as cardiorespiratory gating and CZT detectors have renewed interest by improving spatial resolution and sensitivity. Recent examples of new applications generated by these technical improvements include the localization of left atrial ganglionic plexi, which could aid in the development of more effective catheter ablation procedures for treating atrial fibrillation (39), and detailed assessments of innervation–perfusion mismatch in patients with ischemic heart disease, which could provide valuable insight into patient risk for developing potentially lethal ventricular arrhythmias (38).

Despite the proven utility of $^{123}$I-MIBG SPECT imaging, PET neuronal imaging has gained popularity because of greater tracer variety, superior sensitivity and spatiotemporal resolution, and more developed means of quantification (46,47). PET offers several radiotracers that target predominantly the norepinephrine transporter to image presynaptic sympathetic activity. The earliest norepinephrine transporter–targeted PET radiotracers were $^{11}$C-labeled agents, including $^{11}$C-hydroxyephedrine ($^{11}$C-HED), $^{11}$C-epinephrine, and $^{11}$C-phenylephrine (48). Alterations in the presynaptic uptake of these radiotracers have been demonstrated in numerous cardiac diseases, including heart failure, ischemic heart disease, and arrhythmias (37,48–50).

$^{11}$C-HED, a nonmetabolized analog of norepinephrine, is the most extensively studied radiotracer among the group of $^{11}$C-labeled norepinephrine transporter–targeted radiotracers. Reduced retention of $^{11}$C-HED corresponding to myocardial denervation has been demonstrated in the settings of acute myocardial infarction (42), ischemic (34,37,49,51) and nonischemic cardiomyopathies (51,52), hypertrophic cardiomyopathy (36), and heart failure with preserved ejection fraction (53). In the PAREPET trial (Prediction of Arrhythmic Events with PET) of individuals with ischemic cardiomyopathy, patients who experienced sudden cardiac arrest had greater volumes of denervated myocardium by $^{11}$C-HED PET than did those without cardiac arrest (33% ± 10% vs. 26% ± 11% of the left ventricle; $P = 0.001$) (34). Interestingly, patients with sudden cardiac arrest did not have statistically greater infarct volumes (22% ± 7% vs. 19% ± 9% of the left ventricle; $P = 0.18$) or lower left ventricular ejection fractions (24% ± 8% vs. 28% ± 9% of the left ventricle; $P = 0.053$). In addition, work with $^{11}$C-HED PET in patients with heart failure with a preserved ejection fraction demonstrated that a lower global retention index of $^{11}$C-HED was independently associated with the presence of advanced diastolic dysfunction (grades 2 and 3) in a multivariate logistic regression analysis (odds ratio, 0.66 per 0.01 min$^{-1}$, $P = 0.044$) (53). Despite the established clinical relevance of $^{11}$C-based radiotracers, their popularity has been limited
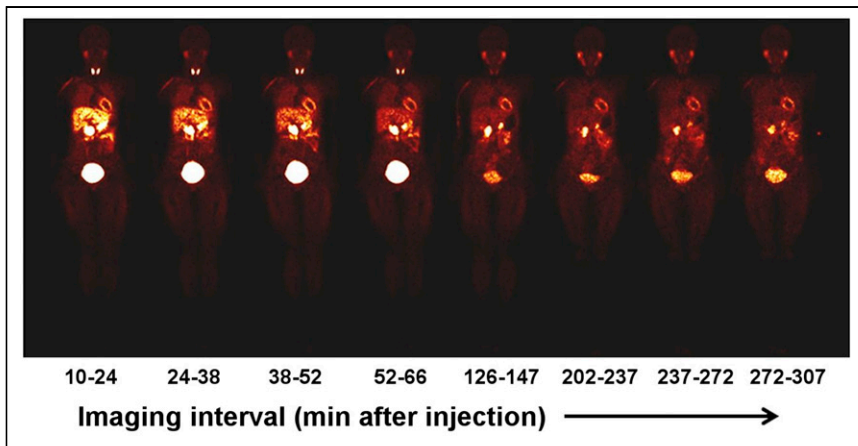
**FIGURE 5.** Presynaptic sympathetic imaging with $^{18}$F-FBBG PET. Figure shows representative sequence of whole-body $^{18}$F-FBBG coronal PET images in healthy volunteer. Myocardial signal persists after clearance from liver and surrounding organs. (Reprinted from (55).)

by a relatively short half-life (20 min) that necessitates on-site cyclotron production.

As a result of the intrinsic limitations of $^{11}$C-based radiotracers, $^{18}$F-based radiotracers targeting the norepinephrine transporter have generated significant interest. $^{18}$F-flubrobenguane ($^{18}$F-FBBG, also known as $^{18}$F-LMI1195) is a benzylguanidine that is similar in structure to $^{123}$I-MIBG (54,55). First-in-humans studies of $^{18}$F-FBBG demonstrated favorable characteristics for imaging, including rapid blood pool clearance, moderate rates of liver and lung clearance, and stable myocardial uptake, with a myocardium-to-liver ratio of more than 2 at 4 h (Fig. 5) (55). Preliminary results of subsequent clinical evaluations demonstrated that $^{18}$F-FBBG yields estimates of myocardial sympathetic innervation similar to those of $^{11}$C-HED but has more favorable kinetics (54). Given the advantages of $^{18}$F-FBBG for quantifying regional myocardial innervation, it was selected for evaluation in the PAREPET II trial to determine the risk of sudden cardiac death in patients with ischemic cardiomyopathy (NCT03493516). In addition to $^{18}$F-FBBG, there are several other $^{18}$F-labeled norepinephrine transporter–targeted radiotracers that are currently in development. $^{18}$F-meta-fluorobenzylguanidine ($^{18}$F-MFBG) is another benzylguanidine with potential for use in cardiac applications; it has demonstrated rapid and sustained myocardial uptake with fast blood pool clearance in initial clinical evaluations (56,57) (NCT02348749). 4-$^{18}$F-fluoro-meta-hydroxyphenethylguanidine and its structural isomer 3-$^{18}$F-fluoro-para-hydroxyphenethylguanidine are phenethylguanidines that were designed for slow neuronal uptake and irreversible presynaptic retention, features thought to be favorable for accurate detection and quantification of cardiac sympathetic denervation (58). First-in-humans studies with these radiotracers demonstrated high-quality images with reproducible measurements of regional cardiac sympathetic nerve density (NCT02669563) (58).

**Postsynaptic Sympathetic Imaging**

$^{11}$C-CGP-12177 (4-(3-tert-butylamino-2-hydroxypropoxy)-2H-benzimidazol-2-$^{11}$C-one) (37,49) and $^{11}$C-CGP-12388 ((S)-4-(3-(2′-$^{11}$C-isopropylamino)-2-hydroxypropoxy)-2H-benzimidazol-2-one) (59,60) are nonselective β-receptor antagonists that have been used for postsynaptic adrenergic imaging. $^{11}$C-CGP-12177 has been paired with presynaptic sympathetic tracers such as $^{123}$I-MIBG (61) and $^{11}$C-HED (36,37,49) to help elucidate the complex relationships between pre- and postsynaptic sympathetic function (Fig. 6). The studies show significant alterations in both pre- and postsynaptic sympathetic function in patients with various types of cardiomyopathies. Chronically increased sympathetic tone in the setting of heart failure is reflected in the decreased uptake or increased washout of presynaptic catecholamines and leads to the observed downregulation of postsynaptic β-adrenergic receptors (61). Although α-adrenergic signaling is less intensively investigated, it also plays a fundamental role in cardiovascular physiology (62) and is an intriguing target for therapeutics and molecular imaging. $^{11}$C-labeled N-[6-[(4-amino-6,7-dimethoxyquinazolin-2-yl)-methyl-amino]hexyl]-N-methylfuran-2-carboxamide;hydrochloride ($^{11}$C-GB67) is a prazosin analog and $\alpha_1$-adrenergic antagonist that has demonstrated myocardial uptake in preclinical and initial human studies, although its clinical role has yet to be established (63,64).

**Parasympathetic Imaging**

Techniques for radioligand imaging of cardiac parasympathetic activity remain far less developed than those for sympathetic imaging despite the central role that parasympathetic innervation plays in cardiovascular physiology. $^{11}$C-donepezil is a reversible, noncompetitive antagonist of acetylcholinesterase that has been investigated in humans as a potential surrogate marker of cardiac parasympathetic innervation (65), although its utility is hindered by donepezil's significant affinity for $\sigma_1$-receptors, which are also plentiful in the heart (66). $^{11}$C-methylquinuclidinyl benzilate is a specific hydrophobic antagonist of muscarinic acetylcholine receptors that has demonstrated significantly greater uptake in patients with dilated cardiomyopathy than in healthy controls (34.5 $\pm$ 8.9 vs. 25.0 $\pm$ 7.7 pmol/mL, $P <$ 0.005) (40). In addition, 2-deoxy-2-$^{18}$F-fluoro-D-glucose-A85380 is a selective agonist of the $\alpha_4\beta_2$ nicotinic receptor that was developed for central nervous system imaging and has demonstrated feasibility in humans for imaging
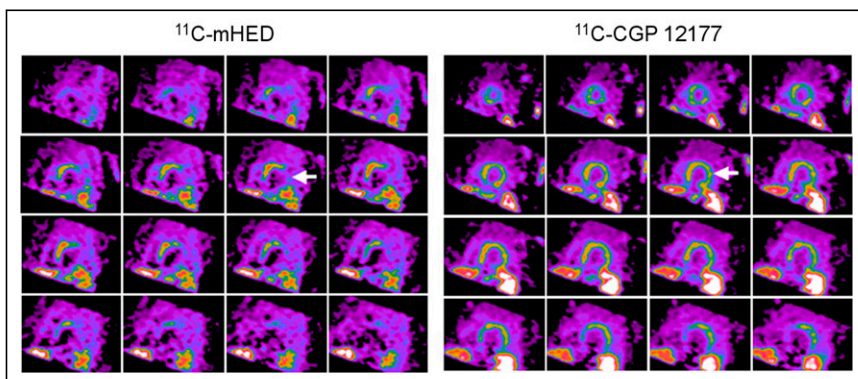


**FIGURE 6.** Pre- and postsynaptic sympathetic imaging with $^{11}$C-HED and $^{11}$C-CGP 12177 PET. Short axis $^{11}$C-HED and $^{11}$C-CGP 12177 PET images of patient with congestive heart failure. Significant pre- and postsynaptic mismatch are noted by arrows. (Reprinted from (49).)

nicotinic receptors in the heart (*67*) and vasculature (*68*). More recently, the vesicular acetylcholine transporter has been investigated as a potential target for radioligand imaging of cardiovascular cholinergic activity. $^{18}$F-fluoroethoxybenzovesamicol is a noncompetitive inhibitor of the vesicular acetylcholine transporter that, in contrast to $^{11}$C-donepezil, has low affinity for $\sigma_1$-receptors (*69*). $^{18}$F-fluoroethoxybenzovesamicol has been extensively studied in the central nervous system and recently demonstrated favorable properties for quantitative cardiac imaging (*69*).

Overall, neuronal radiotracers have thus far not gained widespread use in cardiovascular medicine despite some intriguing preclinical and clinical findings. Multiple technical, clinical, and economic factors likely contribute to the slow advancement of neuronal imaging techniques, including incomplete definitions of their clinical roles and potential added value over established imaging techniques. Given the advantages of PET over SPECT, the field of cardiovascular neuronal imaging will likely continue to shift toward quantitative PET techniques, likely with $^{18}$F-labeled tracers. This will require further development of $^{18}$F-based radiotracers and related quantitative analysis techniques.

## CONCLUSION

Cardiovascular imaging is evolving in response to systemwide trends toward molecular characterization and personalized therapies. The development of new radiotracers for PET and SPECT imaging is central to addressing the numerous unmet diagnostic needs that relate to these changes. Overall, there is a trend toward greater use of PET in cardiovascular medicine given its beneficial imaging properties and established methods for quantification, although SPECT remains highly used because of its favorable cost and availability and the numerous benefits of recent technical improvements. The development of radiotracers for improved characterization of cardiovascular neuronal activity as well as perfusion in both the myocardium and periphery has been discussed in part 1 of this review. Part 2 will present a detailed overview of emerging radiotracers for the imaging of cardiovascular inflammation, fibrosis, thrombosis, calcification, and cardiac amyloidosis.

## REFERENCES

1. Heidenreich PA, Albert NM, Allen LA, et al. Forecasting the impact of heart failure in the United States: a policy statement from the American Heart Association. *Circ Heart Fail.* 2013;6:606–619.
2. Dobrucki LW, Sinusas AJ. PET and SPECT in cardiovascular molecular imaging. *Nat Rev Cardiol.* 2010;7:38–47.
3. Chan C, Harris M, Le M, et al. End-expiration respiratory gating for a high-resolution stationary cardiac SPECT system. *Phys Med Biol.* 2014;59:6267–6287.
4. Fan P, Hutton BF, Holstensson M, et al. Scatter and crosstalk corrections for $^{99m}$Tc/$^{123}$I dual-radionuclide imaging using a CZT SPECT system with pinhole collimators. *Med Phys.* 2015;42:6895–6911.
5. Agostini D, Marie P-Y, Ben-Haim S, et al. Performance of cardiac cadmium-zinc-telluride gamma camera imaging in coronary artery disease: a review from the cardiovascular committee of the European Association of Nuclear Medicine (EANM). *Eur J Nucl Med Mol Imaging.* 2016;43:2423–2432.
6. Thorn SL, Barlow SC, Feher A, et al. Application of hybrid matrix metalloproteinase-targeted and dynamic $^{201}$Tl single-photon emission computed tomography/computed tomography imaging for evaluation of early post-myocardial infarction remodeling. *Circ Cardiovasc Imaging.* 2019;12:e009055.
7. Caobelli F, Wollenweber T, Bavendiek U, et al. Simultaneous dual-isotope solid-state detector SPECT for improved tracking of white blood cells in suspected endocarditis. *Eur Heart J.* 2017;38:436–443.
8. Meoli DF, Sadeghi MM, Krassilnikova S, et al. Noninvasive imaging of myocardial angiogenesis following experimental myocardial infarction. *J Clin Invest.* 2004;113:1684–1691.
9. Holland JP, Williamson MJ, Lewis JS. Unconventional nuclides for radiopharmaceuticals. *Mol Imaging.* 2010;9:1–20.
10. Maddahi J, Lazewatsky J, Udelson JE, et al. Phase-III clinical trial of fluorine-18 flurpiridaz positron emission tomography for evaluation of coronary artery disease. *J Am Coll Cardiol.* 2020;76:391–401.
11. Stendahl JC, Liu Z, Boutagy NE, Nataneli E, Daghighian F, Sinusas AJ. Prototype device for endoventricular beta-emitting radiotracer detection and molecularly-guided intervention. *J Nucl Cardiol.* August 20, 2020 [Epub ahead of print].
12. Conti M, Eriksson L. Physics of pure and non-pure positron emitters for PET: a review and a discussion. *EJNMMI Phys.* 2016;3:8.
13. Calnon DA. Will $^{18}$F flurpiridaz replace $^{82}$rubidium as the most commonly used perfusion tracer for PET myocardial perfusion imaging? *J Nucl Cardiol.* 2019;26: 2031–2033.
14. Maddahi J, Bengel F, Czernin J, et al. Dosimetry, biodistribution, and safety of flurpiridaz F 18 in healthy subjects undergoing rest and exercise or pharmacological stress PET myocardial perfusion imaging. *J Nucl Cardiol.* 2019;26: 2018–2030.
15. Berman DS, Maddahi J, Tamarappoo BK, et al. Phase II safety and clinical comparison with single-photon emission computed tomography myocardial perfusion imaging for detection of coronary artery disease: flurpiridaz F 18 positron emission tomography. *J Am Coll Cardiol.* 2013;61:469–477.
16. Bourque JM, Hanson CA, Agostini D, et al. Assessing myocardial perfusion in suspected coronary artery disease: rationale and design of the second phase 3, open-label multi-center study of flurpiridaz (F-18) injection for positron emission tomography (PET) imaging. *J Nucl Cardiol.* 2021;28:1105–1116.
17. Packard RRS, Lazewatsky JL, Orlandi C, Maddahi J. Diagnostic performance of PET versus SPECT myocardial perfusion imaging in patients with smaller left ventricles: a substudy of the $^{18}$F-flurpiridaz phase III clinical trial. *J Nucl Med.* 2021; 62:849–854.
18. Sogbein OO, Pelletier-Galarneau M, Schindler TH, Wei L, Wells RG, Ruddy TD. New SPECT and PET radiopharmaceuticals for imaging cardiovascular disease. *BioMed Res Int.* 2014;2014:942960.
19. Gewirtz H, Narula J. A closer look at $^{18}$flurpiridaz data in IHD: hiding in plain sight. *J Am Coll Cardiol.* 2020;76:402–404.
20. Bartholomä MD, Zhang S, Akurathi V, et al. $^{18}$F-labeled rhodamines as potential myocardial perfusion agents: comparison of pharmacokinetic properties of several rhodamines. *Nucl Med Biol.* 2015;42:796–803.
21. Shoup TM, Elmaleh DR, Brownell AL, Zhu A, Guerrero JL, Fischman AJ. Evaluation of (4-[$^{18}$F]fluorophenyl)triphenylphosphonium ion. a potential myocardial blood flow agent for PET. *Mol Imaging Biol.* 2011;13:511–517.
22. Wells RG, Wei L, Petryk J, et al. Flow-dependent uptake of $^{123}$I-CMICE-013, a novel SPECT perfusion agent, compared with standard tracers. *J Nucl Med.* 2015; 56:764–770.
23. Broisat A, Ruiz M, Goodman NC, et al. Myocardial uptake of 7′-(Z)-[$^{123}$I]iodorotenone during vasodilator stress in dogs with critical coronary stenoses. *Circ Cardiovasc Imaging.* 2011;4:685–692.
24. Inoue Y, Shirouzu I, Machida T, et al. Collimator choice in cardiac SPECT with I-123-labeled tracers. *J Nucl Cardiol.* 2004;11:433–439.
25. Thompson RC, Heller GV, Johnson LL, et al. Value of attenuation correction on ECG-gated SPECT myocardial perfusion imaging related to body mass index. *J Nucl Cardiol.* 2005;12:195–202.
26. Wells RG, Marvin B, Poirier M, Renaud J, deKemp RA, Ruddy TD. Optimization of SPECT measurement of myocardial blood flow with corrections for attenuation, motion, and blood binding compared with PET. *J Nucl Med.* 2017; 58:2013–2019.
27. Criqui MH, Aboyans V. Epidemiology of peripheral artery disease. *Circ Res.* 2015;116:1509–1526.
28. Alvelo JL, Papademetris X, Mena-Hurtado C, et al. Radiotracer imaging allows for noninvasive detection and quantification of abnormalities in angiosome foot perfusion in diabetic patients with critical limb ischemia and nonhealing wounds. *Circ Cardiovasc Imaging.* 2018;11:e006932.
29. Scholtens AM, Tio RA, Willemsen A, et al. Myocardial perfusion reserve compared with peripheral perfusion reserve: a [$^{13}$N]ammonia PET study. *J Nucl Cardiol.* 2011;18:238–246.
30. Scremin OU, Figoni SF, Norman K, et al. Preamputation evaluation of lower-limb skeletal muscle perfusion with H$_2$ $^{15}$O positron emission tomography. *Am J Phys Med Rehabil.* 2010;89:473–486.
31. Chou TH, Alvelo JL, Janse S, et al. Prognostic value of radiotracer-based perfusion imaging in critical limb ischemia patients undergoing lower extremity revascularization. *JACC Cardiovasc Imaging.* 2021;14:1614–1624.
32. Battipaglia I, Lanza GA. Autonomic innervation of the heart. In: Slart RHJA, Tio RA, Elsinga PH, Schwaiger M, eds. *The Autonomic Nervous System of the Heart.* Springer; 2015:1–12.
33. Le Guludec D, Delforge J, Dolle F. Imaging the parasympathetic cardiac innervation with PET. In: Slart RHJA, Tio RA, Elsinga PH, Schwaiger M, eds. *The Autonomic Nervous System of the Heart.* Springer; 2015:111–135.

34. Fallavollita JA, Heavey BM, Luisi AJ Jr, et al. Regional myocardial sympathetic denervation predicts the risk of sudden cardiac arrest in ischemic cardiomyopathy. *J Am Coll Cardiol.* 2014;63:141–149.

35. Jacobson AF, Senior R, Cerqueira MD, et al. Myocardial iodine-123 meta-iodobenzylguanidine imaging and cardiac events in heart failure: results of the prospective ADMIRE-HF (AdreView Myocardial Imaging for Risk Evaluation in Heart Failure) study. *J Am Coll Cardiol.* 2010;55:2212–2221.

36. Schäfers M, Dutka D, Rhodes CG, et al. Myocardial presynaptic and postsynaptic autonomic dysfunction in hypertrophic cardiomyopathy. *Circ Res.* 1998;82:57–62.

37. John AS, Mongillo M, Depre C, et al. Pre- and post-synaptic sympathetic function in human hibernating myocardium. *Eur J Nucl Med Mol Imaging.* 2007;34:1973–1980.

38. Avendaño R, Hashemi-Zonouz T, Sandoval V, et al. Anger recall mental stress decreases ^{123}I-metaiodobenzylguanidine (^{123}I-MIBG) uptake and increases heterogeneity of cardiac sympathetic activity in the myocardium in patients with ischemic cardiomyopathy. *J Nucl Cardiol.* October 8, 2020 [Epub ahead of print].

39. Stirrup J, Gregg S, Baavour R, et al. Hybrid solid-state SPECT/CT left atrial innervation imaging for identification of left atrial ganglionated plexi: technique and validation in patients with atrial fibrillation. *J Nucl Cardiol.* 2020; 27:1939–1950.

40. Le Guludec D, Cohen-Solal A, Delforge J, Delahaye N, Syrota A, Merlet P. Increased myocardial muscarinic receptor density in idiopathic dilated cardiomyopathy. *Circulation.* 1997;96:3416–3422.

41. Todica A, Siebermair J, Schiller J, et al. Assessment of right ventricular sympathetic dysfunction in patients with arrhythmogenic right ventricular cardiomyopathy: an ^{123}I-metaiodobenzylguanidine SPECT/CT study. *J Nucl Cardiol.* 2020;27:2402–2409.

42. Allman KC, Wieland DM, Muzik O, Degrado TR, Wolfe ER Jr, Schwaiger M. Carbon-11 hydroxyephedrine with positron emission tomography for serial assessment of cardiac adrenergic neuronal function after acute myocardial infarction in humans. *J Am Coll Cardiol.* 1993;22:368–375.

43. Haider N, Baliga RR, Chandrashekhar Y, Narula J. Adrenergic excess, hNET1 down-regulation, and compromised mIBG uptake in heart failure poverty in the presence of plenty. *JACC Cardiovasc Imaging.* 2010;3:71–75.

44. Boutagy NE, Sinusas AJ. Recent advances and clinical applications of PET cardiac autonomic nervous system imaging. *Curr Cardiol Rep.* 2017;19:33.

45. Matsunari I, Aoki H, Nomura Y, et al. Iodine-123 metaiodobenzylguanidine imaging and carbon-11 hydroxyephedrine positron emission tomography compared in patients with left ventricular dysfunction. *Circ Cardiovasc Imaging.* 2010;3:595–603.

46. Bengel FM, Thackeray JT. Altered cardiac innervation predisposes to ventricular arrhythmia: targeted positron emission tomography identifies risk in ischemic cardiomyopathy. *J Am Coll Cardiol.* 2014;63:150–152.

47. Werner RA, Rischpler C, Onthank D, et al. Retention kinetics of the ^{18}F-labeled sympathetic nerve PET tracer LMI1195: comparison with ^{11}C-hydroxyephedrine and ^{123}I-MIBG. *J Nucl Med.* 2015;56:1429–1433.

48. Lautamaki R, Sasano T, Higuchi T, et al. Multiparametric molecular imaging provides mechanistic insights into sympathetic innervation impairment in the viable infarct border zone. *J Nucl Med.* 2015;56:457–463.

49. Caldwell JH, Link JM, Levy WC, Poole JE, Stratton JR. Evidence for pre- to postsynaptic mismatch of the cardiac sympathetic nervous system in ischemic congestive heart failure. *J Nucl Med.* 2008;49:234–241.

50. Sasano T, Abraham MR, Chang KC, et al. Abnormal sympathetic innervation of viable myocardium and the substrate of ventricular tachycardia after myocardial infarction. *J Am Coll Cardiol.* 2008;51:2266–2275.

51. Rijnierse MT, Allaart CP, de Haan S, et al. Sympathetic denervation is associated with microvascular dysfunction in non-infarcted myocardium in patients with cardiomyopathy. *Eur Heart J Cardiovasc Imaging.* 2015;16:788–798.

52. Bengel FM, Permanetter B, Ungerer M, Nekolla SG, Schwaiger M. Relationship between altered sympathetic innervation, oxidative metabolism and contractile function in the cardiomyopathic human heart; a non-invasive study using positron emission tomography. *Eur Heart J.* 2001;22:1594–1600.

53. Aikawa T, Naya M, Obara M, et al. Impaired myocardial sympathetic innervation is associated with diastolic dysfunction in heart failure with preserved ejection fraction: ^{11}C-hydroxyephedrine PET study. *J Nucl Med.* 2017;58:784–790.

54. Zelt JG, Britt D, Mair BA, et al. Regional distribution of fluorine-18-flubrobenguane and carbon-11-hydroxyephedrine for cardiac PET imaging of sympathetic innervation. *JACC Cardiovasc Imaging.* 2021;14:1425–1436.

55. Sinusas AJ, Lazewatsky J, Brunetti J, et al. Biodistribution and radiation dosimetry of LMI1195: first-in-human study of a novel ^{18}F-labeled tracer for imaging myocardial innervation. *J Nucl Med.* 2014;55:1445–1451.

56. Grkovski M, Zanzonico PB, Modak S, Humm JL, Narula J, Pandit-Taskar N. F-18 meta-fluorobenzylguanidine PET imaging of myocardial sympathetic innervation. *J Nucl Cardiol.* January 6, 2022 [Epub ahead of print].

57. Pandit-Taskar N, Zanzonico P, Staton KD, et al. Biodistribution and dosimetry of ^{18}F-meta-fluorobenzylguanidine: a first-in-human PET/CT imaging study of patients with neuroendocrine malignancies. *J Nucl Med.* 2018;59:147–153.

58. Raffel DM, Jung YW, Koeppe RA, et al. First-in-human studies of [^{18}F]fluorohydroxyphenethylguanidines. *Circ Cardiovasc Imaging.* 2018;11:e007965.

59. de Jong RM, Willemsen AT, Slart RH, et al. Myocardial β-adrenoceptor downregulation in idiopathic dilated cardiomyopathy measured in vivo with PET using the new radioligand (S)-[^{11}C]CGP12388. *Eur J Nucl Med Mol Imaging.* 2005;32:443–447.

60. Momose M, Reder S, Raffel DM, et al. Evaluation of cardiac β-adrenoreceptors in the isolated perfused rat heart using (S)-^{11}C-CGP12388. *J Nucl Med.* 2004;45:471–477.

61. Tsukamoto T, Morita K, Naya M, et al. Decreased myocardial β-adrenergic receptor density in relation to increased sympathetic tone in patients with nonischemic cardiomyopathy. *J Nucl Med.* 2007;48:1777–1782.

62. Zhang J, Simpson PC, Jensen BC. Cardiac alpha1A-adrenergic receptors: emerging protective roles in cardiovascular diseases. *Am J Physiol Heart Circ Physiol.* 2021; 320:H725–H733.

63. Law MP, Osman S, Pike VW, et al. Evaluation of [^{11}C]GB67, a novel radioligand for imaging myocardial $\alpha_1$-adrenoceptors with positron emission tomography. *Eur J Nucl Med.* 2000;27:7–17.

64. Park-Holohan SJ, Asselin MC, Turton DR, et al. Quantification of [^{11}C]GB67 binding to cardiac $\alpha_1$-adrenoceptors with positron emission tomography: validation in pigs. *Eur J Nucl Med Mol Imaging.* 2008;35:1624–1635.

65. Gjerløff T, Jakobsen S, Nahimi A, et al. In vivo imaging of human acetylcholinesterase density in peripheral organs using ^{11}C-donepezil: dosimetry, biodistribution, and kinetic analyses. *J Nucl Med.* 2014;55:1818–1824.

66. Horsager J, Fedorova TD, Berge NVD, et al. Cardiac ^{11}C-donepezil binding increases with age in healthy humans: potentially signifying sigma-1 receptor upregulation. *J Cardiovasc Pharmacol Ther.* 2019;24:365–370.

67. Bucerius J, Joe AY, Schmaljohann J, et al. Feasibility of 2-deoxy-2-[^{18}F]fluoro-D-glucose-A85380-PET for imaging of human cardiac nicotinic acetylcholine receptors in vivo. *Clin Res Cardiol.* 2006;95:105–109.

68. Bucerius J, Manka C, Schmaljohann J, et al. Feasibility of [^{18}F]-2-fluoro-A85380-PET imaging of human vascular nicotinic acetylcholine receptors in vivo. *JACC Cardiovasc Imaging.* 2012;5:528–536.

69. Saint-Georges Z, Zayed VK, Dinelle K, et al. First-in-human imaging and kinetic analysis of vesicular acetylcholine transporter density in the heart using [^{18}F]FEOBV PET. *J Nucl Cardiol.* 2021;28:50–54.

70. NuDat 3.0. National Nuclear Data Center website. www.nndc.bnl.gov/nudat2. Accessed March 9, 2022.